Polaritonic critical coupling in a hybrid quasibound states in the continuum cavity–WS_2 monolayer system

Xia Zhang [*] and A. Louise Bradley [†]
School of Physics, CRANN and AMBER, Trinity College Dublin, Dublin 2, Ireland

(Received 22 December 2021; revised 15 March 2022; accepted 24 March 2022; published 21 April 2022)

We theoretically propose and numerically demonstrate that perfect feeding of a polaritonic system with full electromagnetic energy under one-port beam incidence, referred to as polaritonic critical coupling, can be achieved in a hybrid dielectric metasurface–WS_2 monolayer structure. Polaritonic critical coupling, where critical coupling and strong coupling are simultaneously attained, is determined by the relative damping rates of the cavity resonance, γ_Q, provided by a symmetry-protected quasibound states in the continuum cavity, and excitonic resonance of the WS_2 monolayer, γ_X. We reveal that the population of the polariton states can be tuned by the asymmetry parameter of the quasibound states in the continuum. Furthermore, polaritonic critical coupling is achieved in the designed system while $\gamma_Q = \gamma_X$, and only strong coupling is achieved while $\gamma_Q \neq \gamma_X$. This work enriches the study of polaritonic physics with controlled absorbance and may guide the design and application of efficient polariton-based light-emitting or lasing devices.

DOI: 10.1103/PhysRevB.105.165424

I. INTRODUCTION

A photon emitter placed in an optical cavity interacts with the cavity and experiences a change in the photonic density of states. When the interaction rate is slower than their average incoherent dissipation rates, the system operates in the weak-coupling regime [1–4]. However, when the coherent coupling rate dominates, half-light, half-matter bosonic quasiparticles are formed, termed polaritons [5–9]. The system operates in the strong coupling or polaritonic coupling regime. Whatever the regime, weak or strong coupling, maximizing the absorbance is a fundamental property of light-matter interaction and is critical to a wide range of applications, such as photoluminescence enhancement [1,10], nonlinear harmonic generation [11,12], lasing [13–15], and quantum correlations [16,17]. The dissipation of all the electromagnetic energy fed into the system within the system itself corresponds to perfect absorption which occurs when critical coupling is achieved [18]. The underpinning physics of critical coupling is impedance matching [19,20], or the balance of the radiative rate (scattering) with the intrinsic loss rate (dephasing or absorption) of the hybrid system [3,21,22], which does not rely on the coupling strength of the cavity and the emitter. Coherent perfect absorption can be achieved in a single cavity owning coupled resonances [23–25] or in a hybrid cavity-emitter system, supporting the resonant cavity mode and emitter's excitonic resonance [26,27].

To date, critical coupling has been realized and more documented in the weak-coupling regime with a view to tailoring the absorbance bandwidth or magnitude [21,22,28]. However, within the strong-coupling regime, most reports focus on theoretical or experimental demonstration of the generation of exciton-polariton states [6,8,29–33], with only very few reports exploring the absorbance magnitude of polariton states [34–37]. Feeding or pumping the polariton system with maximum electromagnetic energy is vital for the efficiency of polariton-based devices [38]. Pioneering work in Ref. [34] shows that critical coupling and strong coupling can be simultaneously achieved in one system with maximum absorbance by manipulating the coherent rate and damping rate, termed polaritonic critical coupling. Rather than trying to minimize the damping rate to aim for a high-Q cavity, we explore exploiting and tuning the cavity damping rate to achieve critical coupling in the strong-coupling regime.

A dielectric metasurface cavity and two-dimensional monolayer of WS_2 are used as the photonic and excitonic resonators, respectively. Generally, dielectric resonators display an advantage over their plasmonic counterparts due to low Ohmic losses [39,40]. More specifically, a dielectric resonant cavity employing quasibound states in the continuum (QBICs) is chosen as it can control the damping rate through the structure's asymmetry parameter [41–43]; therefore the QBIC structure is ideal for probing the effect of the damping rate in the light-matter interaction. The QBIC structure has displayed extraordinary spatiotemporal field confinement [44]. Moreover, the QBIC cavity has negligible absorbance loss, and the multipolar modes' radiative scattering is dominant. Also in sharp contrast with plasmonic structures employing mainly the electric dipole resonance, magnetic dipole and higher-order quadrupole resonances also play a role, where the coherent interplay of all multipolar modes offers peculiar scattering patterns [45] and thus provides the possibility for inspecting some particular modes for coupling. A WS_2 monolayer is chosen as the two-level atomic emitter due to its direct band gap, high in-plane transition dipole moments, optical stability, and atomic thickness [28,46,47]. The paper is

[*] xzhang@tcd.ie
[†] bradlel@tcd.ie

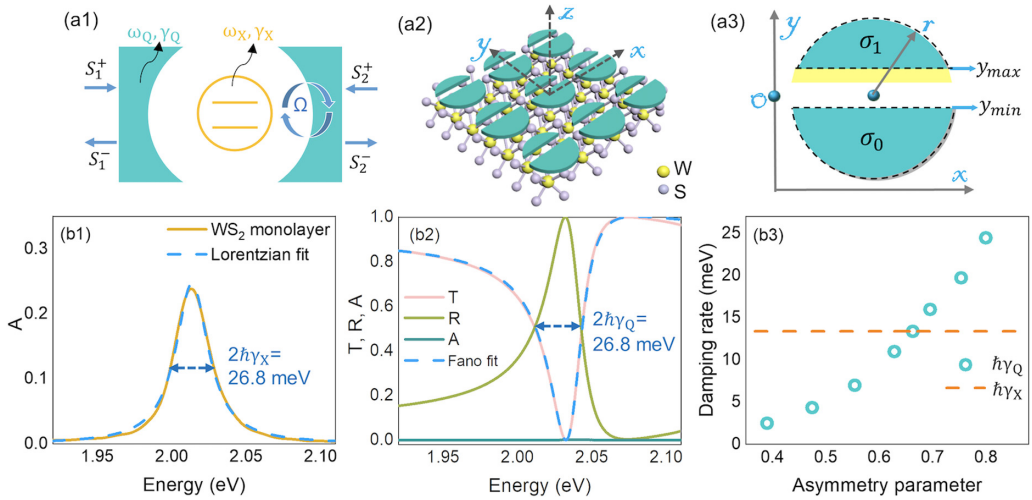

FIG. 1. (a1) Schematic of the coupled cavity-emitter system. A cavity with damping rate γ_Q and resonant frequency ω_Q is coupled to an emitter, with damping rate γ_X and resonant frequency ω_X. Ω is the coupling constant between the emitter and cavity resonators. The hybrid cavity-emitter system can be coupled with m ports, with the example of $m = 2$ shown in the schematic. S^+ and S^- represent the amplitudes of the incoming and outgoing waves at each port. (a2) Schematic of the QBIC cavity-emitter system, which includes monolayer WS_2 as an exciton emitter and a metasurface QBIC gap cavity. The incident beam propagates along z and is polarized along x as $\mathbf{E}_{\text{inc}} = E_0 e^{ik_0 z-\omega t}\mathbf{x}$. (a3) The unit cell of the QBIC gap cavity metasurface. $y_{\min}$ and $y_{\max}$ denote the position of the gap, which is symmetric while $y_{\max} = y_{\min}$; otherwise symmetry breaking exists. r refers to the radius of the disk. The yellow shaded area indicates the reduced disk area σ_1 relative to σ_0 due to symmetry breaking. σ_0 and σ_1 are illustrated as areas delineated by black dashed curves. The asymmetry parameter is calculated as $\alpha = 1 - \sigma_1/\sigma_0$. (b1) Simulated single-beam absorbance spectra of the WS_2 monolayer in air and a Lorentzian fit of the spectrum, from which the spectral width of the exciton resonance, corresponding to the damping rate, is extracted, $2\hbar\gamma_X = 26.8$ meV. (b2) Single-beam reflectance R, transmittance T, and absorbance A spectra of the lossless QBIC metasurface in air, where period $p_x = p_y = 550$ nm, $y_{\min} = -20$ nm, $y_{\max} = 144$ nm, radius $r = 240$ nm, and height $h = 60$ nm. A Fano fit of the transmittance spectrum yields a damping rate of $2\hbar\gamma_Q = 26.8$ meV. (b3) The damping energy of the QBIC metasurface, γ_Q, vs asymmetry parameter α, compared with that of the WS_2 monolayer, γ_X. The damping rates are changed by tuning the asymmetry parameter of the gap cavity, while maintaining the radius of the disk, $r = 240$ nm; the height of the disk, $h = 60$ nm; and $y_{\min} = -20$ nm fixed.

organized as follows. Firstly, within the temporal coupled-mode theory, the conditions for critical coupling, strong coupling, and polaritonic critical coupling are explored. Secondly, a proof-of-concept demonstration that critical coupling and polaritonic critical coupling can be separately achieved in the hybrid QBIC cavity with monolayer WS_2 system is presented. The system is tuned between the different regimes only by varying the damping rate of the QBIC cavity. The contributions of the different multipolar modes within the resonator are also revealed.

II. THEORY

In Fig. 1(a1), a hybrid cavity-emitter system is shown with the example of two ports for incoming and outgoing electromagnetic waves. The system can be described by the temporal coupled-mode theory [48]. The system is driven externally with a coupling constant d. $|Q|$ and $|X|$ denote the amplitude of the photonic mode and the excitonic mode, respectively. The corresponding resonant frequency and damping rate are ω_Q (ω_X) and γ_Q (γ_X), respectively, and they coherently exchange energy with coupling constant, Ω. The incoming wave amplitudes $|S^+\rangle = (S_1^+, S_2^+)$ and the corresponding outgoing wave amplitudes $|S_1^-\rangle$, $|S_2^-\rangle$ are then related by the following equations:

$$\frac{dX}{dt} = (i\omega_X - \gamma_X)X + i\Omega Q,$$

$$\frac{dQ}{dt} = (i\omega_Q - \gamma_Q)Q + i\Omega X + \mathrm{d}^{\mathrm{T}}|s^+\rangle,$$
$$|S^-\rangle = C|S^+\rangle + \mathrm{d}Q, \tag{1}$$

where the incident and outgoing waves are connected as $|S^-\rangle = S(\omega)|S^+\rangle$. d is the coupling constant arranged in vectors. T denotes transposing the row vectors into column vectors. $|Q|^2$ and $|X|^2$ represent the corresponding stored electromagnetic energy. The integration yields

$$S(\omega) = C - \frac{i(\omega - \omega_Q) + \gamma_X}{(\omega - \omega_+)(\omega - \omega_-)}D, \tag{2}$$

where C is the background scattering matrix and $D = |d\rangle(\langle d|)^*$. "*" means only complex conjugation. The expressions for C and D can be gives the coupling constant between resonance modes. The explicit expressions of C and D can be found in Ref. [48].

By calculating Det $S(\omega) = 0$, the upper and lower branches of energy are

$$E_\pm = \hbar\omega_\pm = \frac{\hbar}{2}[\omega_X + \omega_Q + i(\gamma_Q + \gamma_X)]$$
$$\pm \frac{\hbar}{2}\sqrt{4\Omega^2 + [(\omega_X - \omega_Q) + i(\gamma_X - \gamma_Q)]^2}. \tag{3}$$

The vacuum Rabi splitting, defined as the minimum energy spacing between the two branches, is $\hbar\Omega_{\mathrm{R}} = \mathrm{Re}(E_+ - E_-)_{\min}$. When $\omega_X = \omega_Q$ is met, it yields $\hbar\Omega_{\mathrm{R}} =$

$\hbar\sqrt{4\Omega^2-(\gamma_Q-\gamma_X)^2}$. To guarantee the coherent and reversible energy transfer, the energy anticrossing behavior can only be resolved when the Rabi splitting is larger than the total dissipation energy of the hybrid system, $\hbar\Omega_R > \hbar(\gamma_Q + \gamma_X)$ [49–52]. Accordingly, the criteria of strong coupling or polaritonic coupling are

$$\hbar\Omega > \frac{\hbar}{2}|\gamma_Q-\gamma_X|, \quad \hbar\Omega > \hbar\sqrt{\frac{1}{2}\left(\gamma_Q^2+\gamma_X^2\right)}. \tag{4}$$

A special case exists when $\omega_Q = \omega_X$ and $\gamma_X = \gamma_Q$ are simultaneously met. Equation (3) yields $E_\pm = \hbar(\omega_X + i\gamma_X \pm \Omega)$ or $E_\pm = \hbar(\omega_Q + i\gamma_Q \pm \Omega)$, implying the cavity's or emitter's resonance splitting. The derived Rabi splitting energy becomes $\hbar\Omega_R = 2\hbar\Omega$. The criteria of strong coupling according to Eq. (4) become $\hbar\Omega > \hbar\gamma_Q = \hbar\gamma_X$.

Next we consider the critical coupling for the case of a WS_2 monolayer with a QBIC optical resonator. In the case with input only from a single port the energy stored in the optical resonator has a Lorentzian profile with the form $|a|^2 = \gamma_0/[(\omega-\omega_0)^2+\gamma_0^2]$, where a is the amplitude, ω_0 is the resonant frequency, and γ_0 is the damping rate. γ_0 has the contributions of radiative damping (scattering) and nonradiative damping (dephasing, dissipation, or absorption) rates. The bare QBIC cavity has only the radiative scattering rate without dissipative loss. The monolayer WS_2 can be treated as only introducing additional dissipative loss to the QBIC cavity without breaking the mirror symmetry of the cavity resonances due to the ultrathin dimension of the monolayer [21]. The absorbance of the symmetric hybrid system with light incident *via* one port is $A = [1-|\det S(\omega)|^2]/2$ [34,53], which has a maximum absorbance value of 0.5 and sets the criteria for critical coupling. In this paper, the fulfillment of the conditions for strong coupling on $\hbar\Omega_R$ and $\hbar\Omega$ while also achieving a maximum absorbance of 0.5 is referred to as polaritonic critical coupling. The condition for maximum absorbance occurs when the radiative damping rate of the system matches the total of the nonradiative rates which can have a contribution due to nonradiative cavity losses as well as the monolayer WS_2 [34].

III. POLARITONIC CRITICAL COUPLING REALIZATION

Figure 1(a2) shows a schematic of the hybrid structure, where the two-level monolayer WS_2 is in contact with the QBIC cavity. The complex dielectric permittivity of the monolayer WS_2, as a function of the photon energy E is

$$\epsilon(E) = \epsilon_B + \sum_{j=1}^{n}\frac{f_j}{E_{0j}^2 - E^2 - i\Gamma_j E}, \tag{5}$$

where ϵ_B denotes the dielectric permittivity of the background. E_{0j}, f_j, and Γ_j are the resonance energy, the oscillator strength, and the damping rate of the oscillator with index j, respectively. The fit parameters as well as the monolayer thickness are taken from Refs. [47,54] with details listed in Table I.

As seen in Fig. 1(b1), the damping rate of the A-exciton resonance is determined from the calculated absorbance spectrum, $A = 1-R-T$, where a Lorentzian fit is performed. R and T are obtained by Lumerical finite-difference time-domain (FDTD) simulation, where periodic boundary conditions are applied over x-y directions and a perfectly matched layer boundary condition is applied over the z direction. The extracted spectral linewidth is $2\hbar\gamma_X = 26.8$ meV. Correspondingly, $\hbar\gamma_X = 13.4$ meV results from the homogeneous broadening driven by the radiative and nonradiative decay rates; the inhomogeneous broadening is negligible [55].

TABLE I. The fitting parameters for the permittivity of monolayer WS_2.

		$\epsilon_B = 8.76$	
j	f_j [(eV)^2]	E_{0j} (eV)	Γ_j (eV)
1	1.9	2.014	0.029
2	0.254	2.185	0.1
3	0.146	2.25	0.1
4	0.068	2.285	0.1
5	3.07	2.402	0.14
6	1.17	2.575	0.21
7	0.068	2.655	0.21
8	15.5	2.845	0.265
9	12.7	3.047	0.25

As seen in Fig. 1(a3), the designed cavity is a QBIC gap cavity metasurface, where an asymmetric air gap is inserted in the TiO_2 disk resonators. The explored geometry including the periodicity, the gap position, the disk radius, and the height has been selected to guarantee tuning on and off the spectral overlap of the resonance mode with the excitonic resonance to enable energy detuning. The permittivity of TiO_2 is taken from the experimental data in Ref. [56]. More details of the designed gap cavity as well as its QBIC nature can be seen in Ref. [44]. As the WS_2 monolayer excitonic resonance energy E_X is constant, the cavity resonance, E_Q is varied by sweeping only the height of the designed QBIC resonators to enable energy detuning. It is necessary to note that sweeping only the height while maintaining the asymmetry parameter fixed does not affect the damping rate. Generally, the absorbed power of a structure, here the cavity or the WS_2 monolayer, can be quantified by $P_{abs} = \frac{1}{2}\iiint |\mathbf{E}|^2 \mathrm{Im}(\epsilon) dV$ [57], where $|\mathbf{E}|$ is the amplitude of the electric field within the cavity or monolayer WS_2 and ϵ is the corresponding permittivity. The absorbance is in principle the ratio of the total absorbed power within a volume V to the incoming power through the exposed surface area [57,58]. Since the QBIC gap cavity has an infinitesimal imaginary part of the permittivity, the absorbance or dissipation rate of the QBIC cavity is negligible. Therefore the damping rate, γ_Q, of the QBIC cavity purely results from the radiative scattering. The calculated absorbance in Fig. 1(b2) also confirms negligible dissipation losses in the QBIC cavity. The absorbance of the hybrid structure results only from the dissipation losses due to the monolayer WS_2, which is affected by the coupling with the cavity's resonant modes. To explore the coupling between the QBIC cavity and monolayer WS_2, the damping rate of the QBIC cavity is extracted from a Fano fit of the transmission spectrum; an example can be seen in Fig. 1(b2). The Fano fit is performed by $T(E) = T_0 + A_0\frac{[q+2(E-E_0)/E_w]^2}{1+[2(E-E_0)/E_w]^2}$, where E_0 is the resonant energy; E_w is the energy linewidth, or full width at half maximum; T_0 is the transmission offset; A_0 is the continuum-discrete coupling parameter; and q is the Breit-Wigner-Fano parameter.

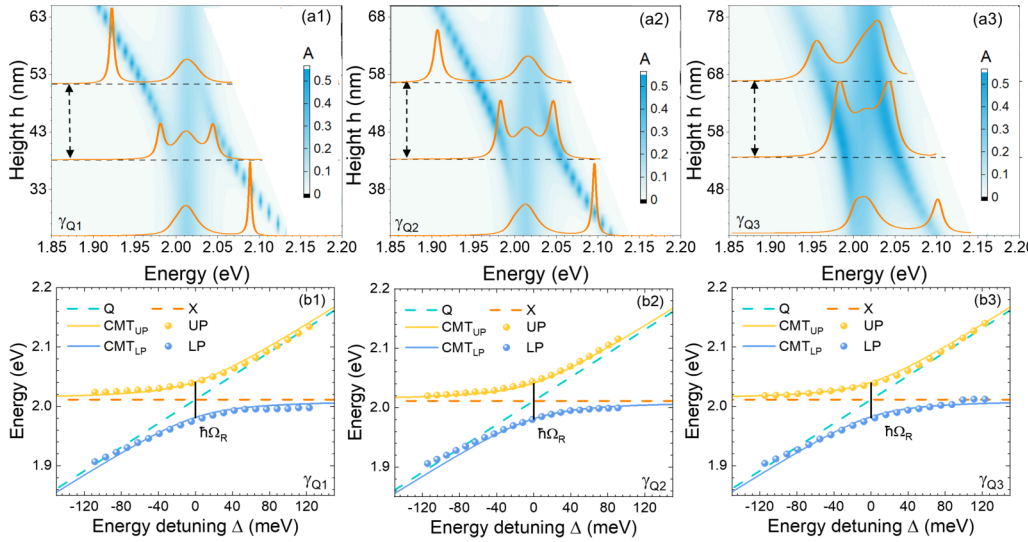

FIG. 2. (a1)–(a3) Polariton dispersion for $\hbar\gamma_{Q1} = 1.5$ meV, $y_{max} = 80$ nm (a1); $\hbar\gamma_{Q2} = 11.4$ meV, $y_{max} = 100$ nm (a2); and $\hbar\gamma_{Q3} = 13.4$ meV, $y_{max} = 144$ nm (a3). The absorbance spectra are shown as a function of the height of the disk. The height of the disk (as labeled) is swept to achieve varied QBIC resonances energies, E_Q, and corresponding energy detuning, $\Delta = E_Q - E_X$. The radius of the disk, $r = 240$ nm, and the gap bottom position, $y_{min} = -20$ nm, are kept constant. The simulated absorbance spectra shown on each dispersion map at the top, middle, and bottom correspond to the cases $E_Q < E_X$, $E_Q = E_X$, and $E_Q > E_X$, respectively. The black dashed lines denote the absorbance scale of 0.5. (b1)–(b3) Peak position as a function of energy detuning for $\hbar\gamma_{Q1} = 1.5$ meV (b1), $\hbar\gamma_{Q2} = 5.7$ meV (b2), and $\hbar\gamma_{Q3} = 13.4$ meV (b3). The red dashed line represents the exciton energy E_X, the dashed blue curve represents the tuned QBIC cavity resonance E_Q, and the two solid curves (CMT_{LP} and CMT_{UP}) are the fitted polariton dispersion of the lower polariton (LP) and upper polariton (UP) branches by using coupled-mode theory (CMT) or Eq. (3). The normal mode splitting, shown by the black solid line, is $\hbar\Omega_R = 64.1$ meV, $\hbar\Omega_R = 63.8$ meV, and $\hbar\Omega_R = 58.9$ meV, respectively.

The calculated absorbance for three damping rates of the QBIC cavity is shown in Figs. 2(a1)–2(a3). The damping rate is determined by the asymmetry parameter, which for the structure in air is shown in Fig. 1(b3). Tuning of the cavity resonance with respect to the exciton energy can be achieved by varying the disk height. As mentioned earlier, varying h does not affect the damping rate. Figures 2(a1)–2(a3) show color maps of the absorbance as a function of energy with varying disk height. Three spectra are shown in each case corresponding to the cases $E_Q < E_X$, $E_Q = E_X$, and $E_Q > E_X$. Due to its high refractive index, the monolayer WS_2 causes an energy redshifting of the QBIC mode [59]. To take account of this effect, the energy of the QBIC mode is simulated by replacing the monolayer WS_2 with an ultrathin nanosheet, which has the same thickness as monolayer WS_2 but with an average refractive index $n = 4.5$ estimated as in Refs. [32,47], which also agrees with the experimental determination in Ref. [60]. The energy of the QBIC mode of the metasurface hybridized with the layer with $n = 4.5$ (E_Q) as well as excitonic energy (E_X) can be seen in Figs. 2(b1)–2(b3). The anticrossing behavior is seen in Fig. 2(b1) for $\hbar\gamma_{Q1} = 1.5$ meV, in Fig. 2(b2) for $\hbar\gamma_{Q2} = 5.7$ meV, and in Fig. 2(b3) for $\hbar\gamma_{Q3} = 13.4$ meV, which is a signature of polaritonic state generation. The upper polariton (UP) and lower polariton (LP) energy branches are well reproduced by Eq. (3). The Rabi splitting energy, corresponding to the minimum value of energy separation between the two branches, indicated by the black solid line, is $\hbar\Omega_R = 64.1$ meV [Fig. 2(b1)], $\hbar\Omega_R = 63.8$ meV [Fig. 2(b2)], and $\hbar\Omega_R = 58$ meV [Fig. 2(b3)]. Comparing the values of $\hbar\Omega_R$, $\hbar\gamma_Q$, and $\hbar\gamma_X$, it yields $\hbar\Omega_R > \hbar(\gamma_Q + \gamma_X)$. Furthermore, the extracted coupling constant according to Eq. (3) is $\hbar\Omega_1 = 32.5$ meV [Fig. 2(b1)], $\hbar\Omega_2 = 32.1$ meV [Fig. 2(b2)], and $\hbar\Omega_3 = 29.5$ meV [Fig. 2(b3)], which all clearly meet the criteria [Eq. (4)] $\hbar\Omega > \hbar|\gamma_Q - \gamma_X|/2$ and $\hbar\Omega > \hbar\sqrt{\frac{1}{2}(\gamma_Q^2 + \gamma_X^2)}$. Therefore polaritonic coupling has been achieved in the hybrid system.

Note that the excitonic absorbance peak $E_X = 2.012$ eV or 616 nm remains visible in the spectra in Figs. 2(a1)–2(a3) due to the presence of nonhybridized excitons remaining in the system [21,61]. For a closer inspection of the absorbance value, the absorbance spectra of the bare and the hybrid structure composed of monolayer WS_2 with the QBIC cavities for the three damping rates of the QBIC cavity can be seen in Fig. 3(a). It is clear that nonhybridized excitons are always present and only some of the exciton population forms polaritons, in particular, for the damping rates of γ_{Q1} and γ_{Q2}. Furthermore, for the case $\gamma_{Q3} = \gamma_X$, the absorbance value increases dramatically compared with the bare WS_2 monolayer, which implies that the population of the excitonic states or the absorbance at E_X is enhanced due to the resonance of the cavity. Particularly, as can be seen in Fig. 2(a3), the absorbance value at the two polariton energies reaches 0.5, which is the maximum possible value that can be obtained for a single input beam, occurring when the condition for strong critical coupling or polaritonic critical coupling is satisfied, namely, when the radiation rate matches the dissipative nonradiative rate in the coupled system. This observation indicates that it should be possible to achieve coherent perfect absorption using two input ports [34]. It is interesting to further inspect the effect of the QBIC cavity's linewidth on the polaritonic coupling, with results shown in Fig. 3(b). It is clear that with

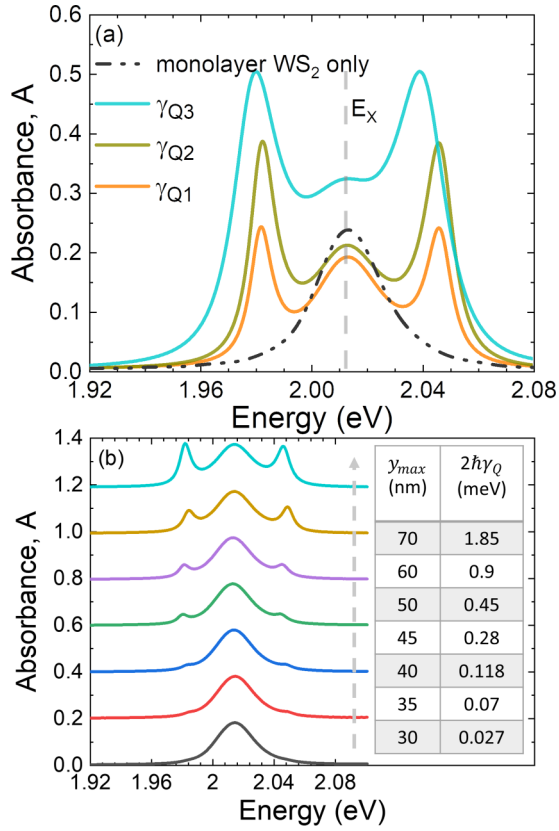

FIG. 3. (a) The calculated absorbance spectra of a bare WS_2 monolayer and the hybrid monolayer WS_2–QBIC cavities for $\hbar\gamma_{Q1} = 1.5$ meV, $\hbar\gamma_{Q2} = 5.7$ meV, and $\hbar\gamma_{Q3} = 13.4$ meV, at resonance where $E_X = E_Q$. The gray dashed line denotes the excitonic peak, E_X. (b) Stacked calculated absorbance spectra of the hybrid monolayer WS_2–QBIC cavities with the value of $y_{\max}$ and $2\hbar\gamma_Q$ shown in the inset. The gray dashed line indicates increasing $y_{\max}$.

increasing damping rates by tuning $y_{\max}$, as indicated by the gray dashed line, the signature of the polaritonic coupling appears and gradually displays a pronounced Rabi splitting. This shows that a minimum required energy linewidth of the cavity for polaritonic coupling with the excitons is at around $y_{\max} = 40$ nm and $2\hbar\gamma_X = 0.118$ meV.

IV. MULTIPOLAR DECOMPOSITION OF QBIC MODES

To get deeper physical insight into the multipolar modes driving the absorbance enhancement and polaritonic critical coupling, multipolar decomposition is performed following Ref. [45], where the calculated electric field is integrated over an area of one unit cell of the array and over the height of the QBIC cavity in the z direction. The amplitude of decomposed multipolar modes contributing to the reflectance or transmittance coefficient of the array is shown in Figs. 4(a1), 4(a2), and 4(a3) for $\hbar\gamma_{Q1} = 1.5$ meV, $\hbar\gamma_{Q2} = 5.7$ meV, and $\hbar\gamma_{Q3} = 13.4$ meV, respectively. The excitonic absorbance spectrum of monolayer WS_2 is also shown to illustrate the spectral width or relative damping rates of the monolayer WS_2 and QBIC modes. It is clear that the total electric dipole, which includes the contributions of the electric dipole **P** and the toroidal dipole $\mathbf{T}_e$, together with the contribution from the magnetic quadrupole **M**, dominates the radiative damping rate of the cavity. The magnetic dipole **m**, magnetic toroidal dipole $\mathbf{T}_m$, and electric quadrupole **Q** are negligible. Moreover, the gradual broadening of the dominant multipolar modes explains the increasing damping rate of QBIC modes [41]. The electric field distribution at the inspected wavelength, which corresponds to the excitonic absorbance peak at $E_X = 2.012$ eV or 616 nm, as well as the field vectors can be seen in Figs. 4(b1)–4(b3). With increasing gap width, or $y_{\max}$, the electric field amplitude decreases, and the trend agrees with the reducing Rabi splitting energy with increasing radiative damping rate. Since the dominant electric dipole **P**, electric toroidal dipole $\mathbf{T}_e$, and magnetic quadrupole **M** have an even parity in the forward and backward scattering plane [45,62], the proposed QBIC gap resonator has a geometric mirror symmetry as well as radial scattering symmetry along the z direction. The damping rate of the QBIC mode is purely driven by the in-plane geometric symmetry breaking along the y direction.

V. SUMMARY

Inspired by a fundamental question within the framework of light-matter coupling regarding maximizing the absorbance of electromagnetic energy for a polaritonic system, a metasurface QBIC cavity is proposed for polaritonic critical coupling, where critical coupling and strong coupling are simultaneously realized. By considering a system composed of a TiO_2 QBIC metasurface optical cavity resonator coupled with the excitons of monolayer WS_2 under single-beam excitation, we have explored the conditions for achieving polaritonic critical coupling. The QBIC cavity enables the manipulation of the damping rates, where the radiative scattering dominates. Through manipulating the relative damping rate of the QBIC cavity and WS_2 monolayer, it is demonstrated that strong coupling and polaritonic critical coupling with absorbance enhancement can be realized for different radiative damping rates. The maximum possible absorbance of 0.5 in the strong-coupling regime is observed when the conditions for polaritonic critical coupling are met. The underlying driving multipolar modes are also explored, revealing that the total electric dipole and magnetic quadrupole dominate the cavity's radially symmetric damping rate. Our study of a WS_2 monolayer interacting with a QBIC resonator with a view to polariton physics may deepen understanding of absorbance manipulation in the strong-coupling regime, spur studies of coherent perfect absorption in a polariton system, and further guide the realization of efficient polaritonic devices.

ACKNOWLEDGMENT

We wish to acknowledge the support of Science Foundation Ireland (SFI) under Grant No. 16/IA/4550.

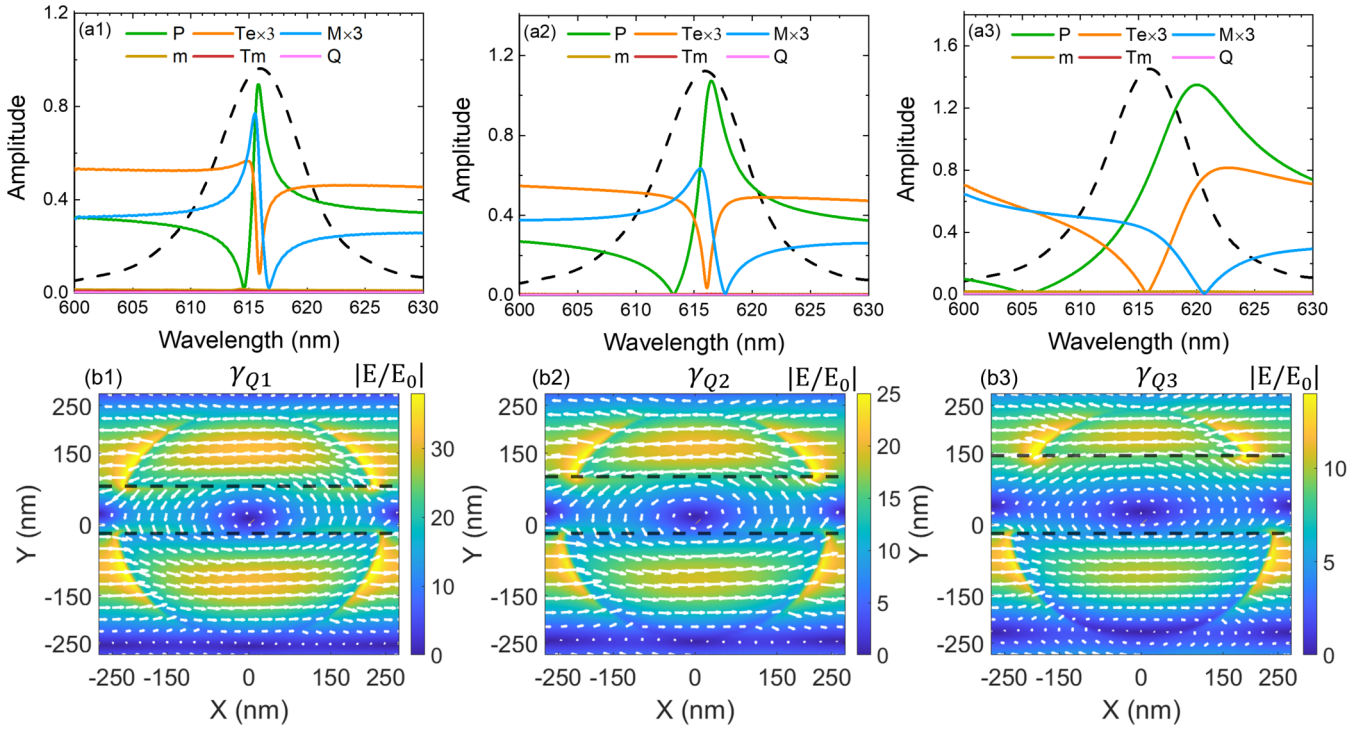

FIG. 4. The amplitude of the decomposed multipolar contributions contributing to the QBIC modes for (a1) $\hbar\gamma_{Q1} = 1.5$ meV, (a2) $\hbar\gamma_{Q2} = 5.7$ meV, and (a3) $\hbar\gamma_{Q3} = 13.4$ meV, including the electric dipole **P**, electric toroidal dipole $\mathbf{T}_e$, magnetic dipole **m**, magnetic toroidal dipole $\mathbf{T}_m$, electric quadrupole **Q**, and magnetic quadrupole **M**. The absorbance spectra (arbitrary units) of monolayer WS_2 are also shown as a black dashed curve, which illustrates the relative spectral linewidth of the exciton and QBIC cavity's contributing modes. (b1)–(b3) The corresponding relative amplitude of the electric field $|\mathbf{E}/\mathbf{E}_0|$ in the x-y plane through the middle of the QBIC cavities. The arrows denote the electric field vectors. The inspected wavelength is at the excitonic peak, $E_X = 2.012$ eV or 616 nm. The black dashed lines indicate the position of the air gap; $y_{\min}$ is kept as -20 nm; and $y_{\max} = 80$ nm for $\hbar\gamma_{Q1}$, $y_{\max} = 100$ nm for $\hbar\gamma_{Q2}$, and $y_{\max} = 144$ nm for $\hbar\gamma_{Q3}$.

[1] S. Kühn, U. Håkanson, L. Rogobete, and V. Sandoghdar, Phys. Rev. Lett. **97**, 017402 (2006).

[2] L. Novotny and N. Van Hulst, Nat. Photonics **5**, 83 (2011).

[3] P. Törmä and W. L. Barnes, Rep. Prog. Phys. **78**, 013901 (2015).

[4] A. G. Curto, G. Volpe, T. H. Taminiau, M. P. Kreuzer, R. Quidant, and N. F. van Hulst, Science **329**, 930 (2010).

[5] A. Trügler and U. Hohenester, Phys. Rev. B **77**, 115403 (2008).

[6] J. Bellessa, C. Bonnand, J. Plenet, and J. Mugnier, Phys. Rev. Lett. **93**, 036404 (2004).

[7] J. Ren, Y. Gu, D. Zhao, F. Zhang, T. Zhang, and Q. Gong, Phys. Rev. Lett. **118**, 073604 (2017).

[8] R. Chikkaraddy, B. De Nijs, F. Benz, S. J. Barrow, O. A. Scherman, E. Rosta, A. Demetriadou, P. Fox, O. Hess, and J. J. Baumberg, Nature (London) **535**, 127 (2016).

[9] E. Peter, P. Senellart, D. Martrou, A. Lemaître, J. Hours, J. M. Gérard, and J. Bloch, Phys. Rev. Lett. **95**, 067401 (2005).

[10] Z. Wang, J. Nie, W. Qin, Q. Hu, and B. Z. Tang, Nat. Commun. **7**, 12033 (2016).

[11] L. Michaeli, S. Keren-Zur, O. Avayu, H. Suchowski, and T. Ellenbogen, Phys. Rev. Lett. **118**, 243904 (2017).

[12] K. Koshelev, S. Kruk, E. Melik-Gaykazyan, J.-H. Choi, A. Bogdanov, H.-G. Park, and Y. Kivshar, Science **367**, 288 (2020).

[13] P. Bhattacharya, T. Frost, S. Deshpande, M. Z. Baten, A. Hazari, and A. Das, Phys. Rev. Lett. **112**, 236802 (2014).

[14] S. De Liberato and C. Ciuti, Phys. Rev. Lett. **102**, 136403 (2009).

[15] S. Wu, S. Buckley, J. R. Schaibley, L. Feng, J. Yan, D. G. Mandrus, F. Hatami, W. Yao, J. Vučković, A. Majumdar, and X. Xu, Nature (London) **520**, 69 (2015).

[16] A. F. Van Loo, A. Fedorov, K. Lalumiere, B. C. Sanders, A. Blais, and A. Wallraff, Science **342**, 1494 (2013).

[17] G. Muñoz-Matutano, A. Wood, M. Johnson, X. V. Asensio, B. Baragiola, A. Reinhard, A. Lemaitre, J. Bloch, A. Amo, B. Besga, M. Richard, and T. Volz, Nat. Mater. **18**, 213 (2019).

[18] H. Haus, *Waves and Fields in Optoelectronics* (Prentice-Hall, Englewood Cliffs, NJ, 1984).

[19] N. I. Landy, S. Sajuyigbe, J. J. Mock, D. R. Smith, and W. J. Padilla, Phys. Rev. Lett. **100**, 207402 (2008).

[20] Y. Ra'di, C. R. Simovski, and S. A. Tretyakov, Phys. Rev. Appl. **3**, 037001 (2015).

[21] J. R. Piper, V. Liu, and S. Fan, Appl. Phys. Lett. **104**, 251110 (2014).

[22] S. Xiao, T. Liu, X. Wang, X. Liu, and C. Zhou, Phys. Rev. B **102**, 085410 (2020).

[23] M. L. Gorodetsky and V. S. Ilchenko, J. Opt. Soc. Am. B **16**, 147 (1999).
[24] M. Cai, O. Painter, and K. J. Vahala, Phys. Rev. Lett. **85**, 74 (2000).
[25] J. R. Tischler, M. S. Bradley, and V. Bulović, Opt. Lett. **31**, 2045 (2006).
[26] H. Noh, Y. Chong, A. D. Stone, and H. Cao, Phys. Rev. Lett. **108**, 186805 (2012).
[27] W. Zhu, F. Xiao, M. Kang, and M. Premaratne, Appl. Phys. Lett **108**, 121901 (2016).
[28] I. Epstein, B. Terrés, A. J. Chaves, V.-V. Pusapati, D. A. Rhodes, B. Frank, V. Zimmermann, Y. Qin, K. Watanabe, T. Taniguchi, H. Giessen, S. Tongay, J. C. Hone, N. M. R. Peres, and F. H. L. Koppens, Nano Lett. **20**, 3545 (2020).
[29] X. Liu, T. Galfsky, Z. Sun, F. Xia, E.-c. Lin, Y.-H. Lee, S. Kéna-Cohen, and V. M. Menon, Nat. Photonics **9**, 30 (2015).
[30] X. Liu, W. Bao, Q. Li, C. Ropp, Y. Wang, and X. Zhang, Phys. Rev. Lett. **119**, 027403 (2017).
[31] P. Xie, D. Li, Y. Chen, P. Chang, H. Zhang, J. Yi, and W. Wang, Phys. Rev. B **102**, 115430 (2020).
[32] S. Cao, H. Dong, J. He, E. Forsberg, Y. Jin, and S. He, J. Phys. Chem. Lett. **11**, 4631 (2020).
[33] J. Lawless, C. Hrelescu, C. Elliott, L. Peters, N. McEvoy, and A. L. Bradley, ACS Appl. Mater. Interfaces **12**, 46406 (2020).
[34] Z. Simone, F. P. Mezzapesa, B. Federica, B. Giorgio, B. Lorenzo, M. S. Vitiello, S. Lucia, C. Raffaele, and A. Tredicucci, Nat. Phys. **10**, 830 (2014).
[35] L. Baldacci, S. Zanotto, G. Biasiol, L. Sorba, and A. Tredicucci, Opt. Express **23**, 9202 (2015).
[36] H. Li, M. Qin, L. Wang, X. Zhai, R. Ren, and J. Hu, Opt. Express **25**, 31612 (2017).
[37] M. Qin, S. Xiao, W. Liu, M. Ouyang, T. Yu, T. Wang, and Q. Liao, Opt. Express **29**, 18026 (2021).
[38] D. Sanvitto and S. Kéna-Cohen, Nat. Mater. **15**, 1061 (2016).
[39] I. Staude and J. Schilling, Nat. Photonics **11**, 274 (2017).
[40] J. T. Hugall, A. Singh, and N. F. van Hulst, ACS Photonics **5**, 43 (2018).
[41] K. Koshelev, S. Lepeshov, M. Liu, A. Bogdanov, and Y. Kivshar, Phys. Rev. Lett. **121**, 193903 (2018).
[42] K. Koshelev, S. Sychev, Z. F. Sadrieva, A. A. Bogdanov, and I. Iorsh, Phys. Rev. B **98**, 161113(R) (2018).
[43] X. Wang, J. Duan, W. Chen, C. Zhou, T. Liu, and S. Xiao, Phys. Rev. B **102**, 155432 (2020).
[44] X. Zhang and A. L. Bradley, arXiv:2104.03463.
[45] A. B. Evlyukhin, T. Fischer, C. Reinhardt, and B. N. Chichkov, Phys. Rev. B **94**, 205434 (2016).
[46] K. F. Mak, C. Lee, J. Hone, J. Shan, and T. F. Heinz, Phys. Rev. Lett. **105**, 136805 (2010).
[47] Y. Li, A. Chernikov, X. Zhang, A. Rigosi, H. M. Hill, A. M. van der Zande, D. A. Chenet, E.-M. Shih, J. Hone, and T. F. Heinz, Phys. Rev. B **90**, 205422 (2014).
[48] S. Fan, W. Suh, and J. D. Joannopoulos, J. Opt. Soc. Am. A **20**, 569 (2003).
[49] V. Savona, L. Andreani, P. Schwendimann, and A. Quattropani, Solid State Commun. **93**, 733 (1995).
[50] H. Deng, H. Haug, and Y. Yamamoto, Rev. Mod. Phys. **82**, 1489 (2010).
[51] L. Zhang, R. Gogna, W. Burg, E. Tutuc, and H. Deng, Nat. Commun. **9**, 713 (2018).
[52] R. Peng, C. Wu, H. Li, X. Xu, and M. Li, Phys. Rev. B **101**, 245418 (2020).
[53] S. Zanotto and A. Tredicucci, Sci. Rep. **6**, 24592 (2016).
[54] P. A. D. Gonçalves, L. P. Bertelsen, S. Xiao, and N. A. Mortensen, Phys. Rev. B **97**, 041402(R) (2018).
[55] S. Wang, S. Li, T. Chervy, A. Shalabney, S. Azzini, E. Orgiu, J. A. Hutchison, C. Genet, P. Samorì, and T. W. Ebbesen, Nano Lett. **16**, 4368 (2016).
[56] S. Sarkar, V. Gupta, M. Kumar, J. Schubert, P. T. Probst, J. Joseph, and T. A. König, ACS Appl. Mater. Interfaces **11**, 13752 (2019).
[57] J. D. Jackson, *Classical Electrodynamics*, 3rd ed. (Wiley, New York, 1999).
[58] G. Baffou, R. Quidant, and C. Girard, Appl. Phys. Lett. **94**, 153109 (2009).
[59] V. Karanikolas, I. Thanopulos, and E. Paspalakis, Phys. Rev. Res. **2**, 033141 (2020).
[60] C. Hsu, R. Frisenda, R. Schmidt, A. Arora, S. M. de Vasconcellos, R. Bratschitsch, H. S. van der Zant, and A. Castellanos-Gomez, Adv. Opt. Mater. **7**, 1900239 (2019).
[61] E. S. Kang, S. Chen, S. Sardar, D. Tordera, N. Armakavicius, V. Darakchieva, T. Shegai, and M. P. Jonsson, ACS Photonics **5**, 4046 (2018).
[62] X. Zhang and A. L. Bradley, Phys. Rev. B **103**, 195419 (2021).